

The 21-cm signals from ultracompact minihaloes as a probe of primordial small-scale fluctuations

Kunihiko Furugori¹, Katsuya T.Abe, Toshiyuki Tanaka, Daiki Hashimoto, Hiroyuki Tashiro and Kenji Hasegawa

¹*Division of Particle and Astrophysical Sciences, Graduate School of Science, Nagoya University, Furocho Chikusa, Nagoya, 464-8602, Aichi, Japan*

4 August 2020

ABSTRACT

Ultracompact minihaloes (UCMHs) can form after the epoch of matter-radiation equality, if the density fluctuations of dark matter have significantly large amplitude on small scales. The constraint on the UCMH abundance allows us to access such small-scale fluctuations. In this paper, we present that, through the measurement of 21-cm fluctuations before the epoch of reionization, we can obtain a constraint on the UCMH abundance. We calculate the 21-cm signal from UCMHs and show that UCMHs provide the enhancement of the 21-cm fluctuations. We also investigate the constraint on the UCMH abundance and small-scale curvature perturbations. Our results indicate that the upcoming 21-cm observation, the Square Kilometre Array (SKA), provides the constraint on amplitude of primordial curvature power spectrum, $\mathcal{A}_\zeta \lesssim 10^{-6}$ on $100 \lesssim k \lesssim 1000 \text{ Mpc}^{-1}$. Although it is not stronger than the one from the non-detection of gamma-rays induced by dark matter annihilation in UCMHs, the constraint by the SKA will be important because this constraint is independent of the dark matter particle model.

Key words: cosmic background radiation – dark ages – reionization – first stars – inflation – large-scale structure of Universe

1 INTRODUCTION

Recent developments of cosmological observations allow us to access the detailed nature of the seeds of galaxies, galaxy clusters and large-scale structures. The precise measurement of the anisotropy in the cosmological microwave background (CMB) radiation strongly shows that the statistical property of the seeds can be expressed in the almost scale-invariant power spectrum of the curvature perturbations with the amplitude $\mathcal{A}_\zeta \sim 10^{-9}$ (Planck Collaboration et al. 2018), which is consistent with the prediction in the inflation paradigm (Guth & Pi 1982; Bardeen et al. 1983). The observations of Lyman-alpha forest support that this tendency is confirmed up to the wave number $k \sim 1 \text{ Mpc}^{-1}$ (McDonald et al. 2006; Bird et al. 2011). However, probing the perturbations below Mpc scales is still a challenge. Currently we have the upper limit on the amplitude of the small-scale amplitude through the constraint on the CMB distortions (Chluba et al. 2012; Dent et al. 2012), the primordial black hole abundance (Josan et al. 2009 and see references therein) and gravitational waves, though these constraints are weaker than those on large scales (see Emami & Smoot 2018 for review).

Now ultracompact minihaloes (UCMHs) draw attention to access the perturbations on such small scales. UCMHs

are predicted to form with the excess power on small scales (Ricotti & Gould 2009). The dark matter density fluctuations can grow after entering the horizon even before the epoch of radiation-matter equality. Therefore, the overdensity regions with the density fraction $\delta > 10^{-3}$ at the horizon entry can collapse to minihaloes around $z \sim 1000$ well before the standard structure formation history. Since UCMHs could be formed by the radial infalling in high redshifts, UCMHs are assumed to have a more compact profile with a larger central density than typical dark matter halos in the standard hierarchical structure formation (Ricotti & Gould 2009). The first cosmological simulation of the UCMH formation has been done by Gosenca et al. (2017). They showed that a large amplitude on small scales leads to the early structure formation and the resultant dark matter halos have a large density. Recent numerical simulations by Delos et al. (2018a,b) showed that UCMHs originated from the spike-shape spectrum on small scales have the Moore profile, $\rho \propto r^{-3/2}$ at the inner cusp region (Moore et al. 1999), which is steeper than the Navarro-Frenk-White (NFW) profile (Navarro et al. 1995).

If the dark matter is a weakly interacting massive particle (WIMP) (Steigman & Turner 1985; Jungman et al. 1996; Kolb et al. 1999), then UCMHs can become cosmo-

logical gamma-ray sources because the signal of the annihilation of WIMPs is enhanced in the dense region at the centre of UCMHs. Currently, the non-detection of the gamma-ray emission from the WIMP annihilation provides the constraint on the UCMH abundance and the stringent constraints on the small-scale curvature power spectrum, $A_\zeta < 10^{-7}$ for $10 < k < 10^8 \text{ Mpc}^{-1}$ (Josan & Green 2010; Scott & Sivertsson 2010; Bringmann et al. 2012; Clark et al. 2016; Nakama et al. 2018; Delos et al. 2018a,b). The non-detection of neutrino from the WIMPs also provides a similar constraint (Yang et al. 2013; Nakama et al. 2018). The Thomson scattering optical depth for the CMB photons also provides the UCMH abundance because the annihilation gamma-ray from UCMHs can contribute to the photon budget for cosmic reionization (Zhang 2011; Yang et al. 2011; Yang 2016; Clark et al. 2017). Observations of gravitational lensing by UCMHs also constraint the UCMH abundance (Li et al. 2012; Clark et al. 2016).

The aim of this paper is to demonstrate that future 21-cm observations can provide the constraint on the UCMH abundance and small-scale curvature power spectrum, which does not require the dark matter particle model. The measurements of 21-cm line emitted by hyperfine transition of neutral hydrogen from high redshifts universe are expected to be a powerful tool to probe the structure formation during the dark ages to the epoch of reionization (EoR) (Furlanetto et al. 2006). The signal amplitude strongly relates to the spatial distribution of neutral hydrogen in the intergalactic medium (IGM) and collapsed objects. The 21-cm observations can probe the IGM matter fluctuations on much smaller scales than the Silk scales (Loeb & Zaldarriaga 2004). Minihaloes which formed in the early stage of the hierarchical structure formation history, are also promised source of 21-cm signal in high redshifts (Iliev et al. 2002; Furlanetto & Oh 2006). Recent studies have shown that the measurements of their signals by future observations provide the detailed stochastic nature of small-scale density fluctuations including the running spectrum, non-Gaussianity and so on (Chongchitnan & Silk 2012; Sekiguchi et al. 2018, 2019). It was also suggested that 21-cm observations can provide the limit on the Primordial Black Hole (PBH) abundance indirectly (Mack & Wesley 2008; Tashiro & Sugiyama 2013). Nowadays, several projects are conducting observation to detect the 21-cm fluctuations around and before the EoR, e.g., the Low Frequency Array (van Haarlem et al. 2013), the Giant Meterwave Radio Telescope (Paciga et al. 2011), the Murchison Widefield Array (Tingay et al. 2013; Bowman et al. 2013) and the Precision Array for probing the EoR (Parsons et al. 2010). Since the measurement of 21-cm fluctuations through these observations is very difficult, there are only the upper limit on the 21-cm fluctuations (Patil et al. 2017; Paciga et al. 2013; Ali et al. 2015; Beardsley et al. 2016; Li et al. 2019). However, it is expected that the high sensitivity of the future instrument, the Square Kilometre Array (SKA), can measure the 21-cm fluctuations up to the redshift $z \sim 28$ (Koopmans et al. 2015).

In this paper, we discuss the possibility of SKA to measure the 21-cm fluctuations originated in UCMHs. Constructing the baryon gas model in UCMHs, we first evaluate the 21-cm fluctuations created by UCMHs. Then we evalu-

ate the detectability of these 21-cm fluctuations by the SKA and discuss the possible constraint on both of the UCMH abundance and the small-scale primordial curvature perturbations.

This paper is organised as follows. In section 2, we present a brief review about UCMHs. In section 3, we construct the baryon gas model in UCMHs considering the hydrostatic equilibrium with the compact dark matter profile in UCMHs. Then we evaluate the 21-cm signal from an individual UCMH. In section 4, we calculate the 21-cm fluctuations due to the UCMHs distribution. We also discuss the detectability of these fluctuations by the SKA. Based on the discussion, we provide the possible constraint on the UCMHs and the primordial curvature perturbations. Finally we give a conclusion of this paper in section 5.

Throughout this paper we assume the flat Λ CDM cosmology with Hubble constant $h = 0.701$, matter density $\Omega_m = 0.1408h^{-2}$, baryon density $\Omega_b = 0.022h^{-2}$, dark matter density $\Omega_{\text{dm}} = 0.1187h^{-2}$, scale invariant spectral index $n_s = 0.965$, and power spectrum normalized factor $\sigma_8 = 0.8$.

2 UCMHS WITH THE SPIKED MATTER SPECTRUM

Small-scale matter density fluctuations with larger amplitude can be seeds of UCMHs. In this section, we begin with the brief review of UCMHs with the spiky shape power spectrum, according to Delos et al. (2018a,b).

Adding on to the nearly scale-invariant spectrum, we consider the spike shape of the primordial curvature power spectrum on a small scale, which enters the horizon during the radiation dominated era,

$$\mathcal{P}_\zeta(k) = \mathcal{A}_\zeta k_s \delta(k - k_s), \quad (1)$$

where \mathcal{A}_ζ is the amplitude of the spike shape and k_s is the wave number of the spike. During the radiation dominated era, the dark matter fluctuations can grow logarithmically. Here, for simplicity, we adopt the Dirac delta function to represent the additional spike-shape spectrum. Then after the radiation-matter equality, they evolve proportionally to the scale factor. When the density amplitude in a overdensity region reaches the critical value for the collapse, the overdensity region can collapse to a dark matter halo as the standard hierarchical structure formation.

However, when the spike amplitude is much larger than one of the ordinary scale-invariant spectrum, the properties of the resultant dark matter halo are different from that of the standard dark matter halos. N-body simulations by Delos et al. (2018b) showed that the spike spectrum produces the isolated distribution of compact dark matter halos, that is UCMHs. The resultant dark matter density profile in a UCMH is represented by a self-similar form as

$$\rho_{\text{dm}}(r) = \rho_s y_{\text{dm}} \left(\frac{r}{r_s} \right), \quad (2)$$

where r is the radial distance from the centre, ρ_s is the scale density and r_s are the scale radius. The non-dimensional density profile y_{dm} is given by

$$y_{\text{dm}}(x) = \frac{1}{x^\alpha (1+x)^{3-\alpha}}, \quad (3)$$

with defining $x \equiv r/r_s$. The simulations demonstrated that

the index α for UCMHs is $\alpha = 1.5$, that is the Moore profile (Moore et al. 1999). It is known that the hierarchical structure formation yields the NFW profile (Navarro et al. 1995) whose index corresponds to $\alpha = 1$. Therefore, UCMHs have a steeper dark matter profile in the inner region.

Delos et al. (2018b) also showed that ρ_s and r_s are related to the UCMH forming redshift z_c and the wave number of the spike as

$$\rho_s = 30(1 + z_c)^3 \Omega_m \rho_{\text{crit},0} \quad (4)$$

$$r_s = 0.7[(1 + z_c)k_s]^{-1}, \quad (5)$$

where $\rho_{\text{crit},0}$ is the critical density at present.

For the UCMH (virial) mass, M_{vir} , we adopt the mass enclosed within r_{200} ,

$$M_{\text{vir}} = 4\pi\rho_s r_s^3 m(u_\nu), \quad (6)$$

$$m(x) \equiv \int_0^x u^2 y_{\text{dm}}(u) du. \quad (7)$$

where u_ν is $u_\nu \equiv r_{200}/r_s$ and the scale r_{200} is defined as the scale inside which the averaged dark matter density is 200 times the mean dark matter density of the Universe. We found that the UCMH mass is related to z_c and k_s as in

$$M_{\text{vir}} \sim 4 \times 10^3 M_\odot \times \left(\frac{k_s}{10^3 \text{ Mpc}^{-1}} \right)^{-3} \ln \left(\frac{1 + z_c}{1} \right). \quad (8)$$

Therefore, the virial mass of a UCMH grows logarithmically even after the formation of the UCMH. This growth corresponds to the late-time accretion on the outer region suggested in the simulation (Delos et al. 2018b). The number density of UCMHs can be evaluated from the peak theory (Bardeen et al. 1986), because UCMHs form at the peak locations of the density fluctuations following the peak shape spectrum. The differential UCMH number density by the formation redshift z_c can be expressed in

$$\frac{dn}{dz_c} = \frac{k_s^3}{1 + z_c} h \left[\frac{\delta_c}{\sigma_d(z_c)} \right], \quad (9)$$

where δ_c is the critical density contrast for collapse, $\delta_c = 1.68$. $\sigma_d(z)$ is the root-mean-squared (rms) variance of the density fluctuation given by the peak shape spectrum at the redshift z . In equation (9), $h(\nu)$ is given by

$$h(\nu) = \frac{\nu}{(2\pi)^{2/3} e^{-\nu^2/2}} f(\nu). \quad (10)$$

where $f(\nu)$ is provided in equation (A15) of Bardeen et al. (1986). For the detailed derivation of equation (9), we refer readers to the appendix in Delos et al. (2018b). Through equation (9), the abundance of UCMHs is related to the spike shape properties, \mathcal{A}_ζ and k_s . Hence, once we obtain the constraint on the abundance of UCMHs, we can provide the limit on the peak-shape spectrum through equation (9).

3 TWENTY ONE CM SIGNAL FROM A SINGLE UCMH

In this section, we evaluate the 21-cm signal from a single UCMH. The 21-cm signal is sensitive to the gas density profile in a UCMH. Therefore, we first derive the profile in a UCMH assuming the hydrostatic equilibrium with the gravitational potential of the dark matter profile presented in the previous section.

3.1 Baryon gas mass in UCMHs

Baryonic density fluctuations, unlike the dark matter, cannot grow before the decoupling of photons. After the decoupling, the baryon density fluctuations start to evolve, following the dark matter density fluctuations. However, since the baryon gas resists the gravitational collapse, there is the critical scale for the collapse, the so-called Jeans scale. Therefore, to evaluate the baryon gas mass inside UCMHs, we consider two scenarios depending on the spike scale, k_s .

When k_s is smaller than the Jeans wave number, k_J , the baryon density fluctuations with k_s can grow and collapse, following the dark matter density evolution. Therefore, for simplicity, we assume that UCMHs can have the baryon gas whose mass ratio to dark matter is the same as the ratio of the cosmological background,

$$M_{\text{gas}}(z) = \frac{\Omega_b}{\Omega_{\text{dm}}} M_{\text{vir}}(z) \quad (\text{for } k_s < k_J). \quad (11)$$

On the other hand, when k_s is larger than k_J , the baryon density fluctuations with k_s cannot evolve due to its own pressure. However, UCMHs can host dense baryon gas through the accretion of baryon gas. We obtain the accreted baryon gas mass at the redshift z from

$$M_{\text{gas}}(z) = \int_z^{z_{\text{acc}}} dz' \frac{\dot{M}_{\text{gas}}(z')}{(1 + z')H(z')} \quad (\text{for } k_s > k_J), \quad (12)$$

where z_{acc} is the starting redshift of the gas accretion. We set z_{acc} to $z_{\text{acc}} = \min[z_c, z_{\text{dec}}]$ where z_{dec} is the redshift for the decoupling of photons. For the accretion rate, $\dot{M}_{\text{gas}}(z)$, we adopt the Bondi-Hoyle-Lyttleton accretion (Bondi & Hoyle 1944),

$$\dot{M}_{\text{gas}}(z) = 4\pi G^2 \Omega_b \rho_{\text{crit}}(z) M_{\text{vir}}^2(z) v_r^{-3}(z). \quad (13)$$

Here v_r is the relative velocity between baryon and dark matter, $v_r(z) = 30 \text{ kms}^{-1} [(1 + z)/1000]$ (Tseliakhovich & Hirata 2010)¹. Note that, to avoid the over-accretion to UCMHs, we set the upper limit of the accretion gas mass, $M_{\text{gas}} < M_{\text{vir}} \Omega_b / \Omega_{\text{dm}}$.

In figure 1, we plot the baryon gas mass ratio to the dark matter mass in UCMHs, $f_{\text{mass}} = M_{\text{gas}}/M_{\text{vir}}$, at the redshift $z = 20$ as a function of the spike wave number k_s . The black solid, dashed and dotted lines represent f_{mass} for UCMHs collapsed at $z_c = 50, 100, \text{ and } 1000$, respectively. For reference, we plot the Jeans wave number at $z = 20$ in the blue thin vertical line. Through this paper, we adopt the Jeans wave number in (Barkana & Loeb 2001).

When the spike wave number is smaller than k_J we assume that the baryon can collapse following the dark matter. Therefore, the gas mass ratio is $f_{\text{mass}} = \Omega_b / \Omega_{\text{dm}}$ as shown in equation (11). On the other hand, when $k_s > k_J$, UCMHs obtain the baryon gas through the accretion with the accretion rate in equation (13). Since the accretion rate is proportional to $M_{\text{vir}}^2 \propto k_s^{-6}$, the baryon gas mass steeply declines with increasing k_s . Figure 1 also shows that a UCMH with

¹ Here, we neglect the contribution of the baryon thermal velocity, which is smaller than the relative velocity between baryon and dark matter (Tseliakhovich & Hirata 2010). The peak spectrum also causes the additional relative velocity. However, the velocity is suppressed by the wave number k . Therefore, we also neglect this contribution.

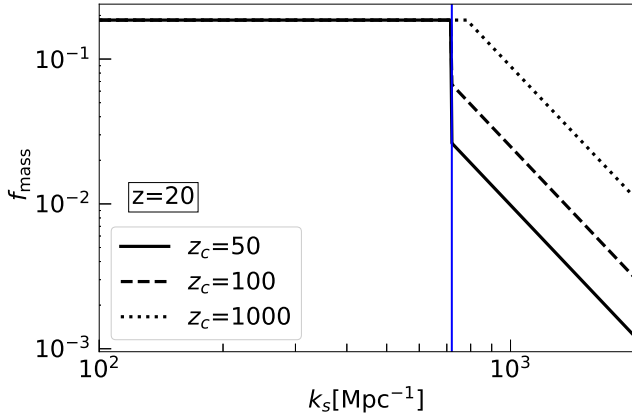


Figure 1. Baryon gas mass ratio to the dark matter mass, $f_{\text{mass}} = M_{\text{gas}}/M_{\text{vir}}$, at the redshift $z = 20$. The solid, dashed, and dotted black lines show the baryon gas mass fraction of the UCMH formed at $z_c = 50$, 100, and 1000, respectively. We also provide the Jeans wave number at $z = 20$ in a vertical blue line.

large z_c has high gas mass ratio. When the UCMH formation happens in higher redshifts, the UCMH undergoes the long duration of the accretion. As a result, the earlier the UCMH forms, the larger the accreted gas mass is in the UCMH.

3.2 Baryon gas density and temperature in UCMHs

Now we evaluate the density and temperature profiles of the baryon gas following the method of [Komatsu & Seljak \(2001\)](#), which is based on the hydrostatic equilibrium assumption.

Since the dark matter profile is expressed in the self-similar form, the gas density profile of UCMHs, ρ_{gas} , would also be the self-similar form as

$$\rho_{\text{gas}}(r) = \rho_{\text{gas}}(0) y_{\text{gas}} \left(\frac{r}{r_s} \right), \quad (14)$$

where $y_{\text{gas}}(x)$ is the non-dimensional gas profile normalized as $y_{\text{gas}}(0) = 1$. Applying the polytropic gas model with the polytropic index γ , we can write the gas temperature profile in

$$T_{\text{gas}}(r) = T_{\text{gas}}(0) y_{\text{gas}}^{\gamma-1} \left(\frac{r}{r_s} \right). \quad (15)$$

The assumption of the hydrostatic equilibrium allows us to relate the gas pressure profile to the dark matter density profile,

$$\rho_{\text{gas}}^{-1} \frac{dP_{\text{gas}}}{dr} = -\frac{GM(r)}{r^2}. \quad (16)$$

Here we assume that the gas component does not contribute to the gravitational potential. To derive the pressure profile, we adopt the equation of state of ideal gas,

$$P_{\text{gas}} = \frac{k_B T_{\text{gas}}}{\mu m_p} \rho_{\text{gas}}, \quad (17)$$

where k_B is the Boltzmann constant, m_p is the proton mass and μ is the mean molecular weight of the gas. Using equations (15) and (16), y_{gas} can be derived as ([Suto et al. 1998](#))

$$y_{\text{gas}}^{\gamma-1}(x) = 1 - 3\eta_0^{-1} \frac{\gamma-1}{\gamma} \frac{u_v}{m(u_v)} \int_0^x du \frac{m(u)}{u^2}, \quad (18)$$

where the mass-temperature normalization factor η_0 is expressed as

$$\eta_0 = \frac{3k_B r_{200} T_{\text{gas}}(0)}{G\mu m_p M_{\text{vir}}}. \quad (19)$$

To obtain the gas profile, it is required to fix η_0 and γ . For the determination of these parameters, we take the assumption that the gas profile traces the dark matter profile outside halo core. This condition is satisfied by imposing the slopes of these two profiles to match,

$$s_* \equiv \left. \frac{d \ln \rho_{\text{dm}}(x)}{d \ln x} \right|_{x=x_*} = \left. \frac{d \ln \rho_{\text{gas}}(x)}{d \ln x} \right|_{x=x_*}, \quad (20)$$

where x_* is the location outside the core region. As a result, we obtain

$$\gamma = 1 - \frac{1}{s_*} + \frac{\partial \ln[m(x_*)/s_*]}{s_* \partial \ln x_*}, \quad (21)$$

$$\eta_0 = 3\gamma^{-1} \left[\left(\frac{-1}{s_*} \right) \left[\frac{x_*^{-1} m(x_*)}{u_v^{-1} m(u_v)} \right] + (\gamma-1) \frac{u_v}{m(u_v)} \int_0^{x_*} du \frac{m(u)}{u^2} \right], \quad (22)$$

where s_* is provided from the dark matter distribution,

$$s_* = - \left[\alpha + (3-\alpha) \frac{x_*}{1+x_*} \right]. \quad (23)$$

One can see that η_0 is a function of x_* and γ . It is preferable that η_0 does not depend on the location x_* . To satisfy this condition, we impose the following condition, according to [Komatsu & Seljak \(2002\)](#),

$$\frac{\partial \eta_0}{\partial x_*} = 0, \quad (24)$$

with setting $x_* = u_v$. This equation yields

$$\gamma = \frac{16u_v^2 + 20u_v + 5}{3(1+2u_v)^2} - \frac{2u_v}{3(1+2u_v)m(u_v)} \left(\frac{u_v}{1+u_v} \right)^{1/2}, \quad (25)$$

where $m(x)$ is given by

$$m(x) = 2 \ln(\sqrt{x} + \sqrt{1+x}) - 2 \sqrt{\frac{x}{1+x}}. \quad (26)$$

The final parameter to determine the gas profile is $\rho_{\text{gas}}(0)$, which we obtain through

$$\rho_{\text{gas}}(0) = M_{\text{gas}} \left[4\pi r_s^3 \int_0^{u_v} y_{\text{gas}}(u) u^2 du \right]^{-1}, \quad (27)$$

where M_{gas} is given in equations (11) and (12).

3.3 Brightness temperature

Let us evaluate the 21-cm signal of a single UCMH at z . First we consider a line of sight intersecting the UCMH with the impact parameter α_R (in unit of r_{200}) from its centre. The brightness temperature along this line of sight is given by

$$T_b(\alpha_R) = T_{\text{CMB}}(z) e^{-\tau(\alpha_R)} + \int_{-R_{\text{max}}}^{R_{\text{max}}} T_s(l) e^{-\tau(\alpha_R, R)} \frac{d\tau}{dR} dR,$$

(28)

where $T_{\text{CMB}}(z) = T_{\text{CMB},0}(1+z)$ with $T_{\text{CMB},0} = 2.73$ K, R is the coordinate along the line of sight, whose origin is set to the centre of the UCMH, T_s is the radial profile of the spin temperature in the UCMH (we will discuss later), l represents the radial distance satisfying $l^2 = R^2 + (\alpha_R r_{200})^2$ and R_{max} is defined as $R_{\text{max}}^2 \equiv r_{200}^2(1 - \alpha_R^2)$.

The optical depth, $\tau(R)$, for the frequency at the rest frame of the UCMH, ν , is calculated from

$$\tau(\alpha_R, R) = \frac{3c^2 A_{10} T_*}{32\pi\nu_*^2} \int_{-R_{\text{max}}}^R \frac{n_{\text{Hi}}(l)\phi(\nu, l)}{T_s(l)} dR, \quad (29)$$

where T_* is $T_* = 0.0681$ K and $\nu_* = 1440$ MHz, A_{10} represents the Einstein A coefficient for the 21-cm transition, $A_{10} = 2.85 \times 10^{-15} \text{s}^{-1}$, and $n_{\text{Hi}}(r)$ provides the radial profile of neutral hydrogen which we obtain through $n_{\text{Hi}}(r) = (1 - Y)\rho_{\text{gas}}/m_p$ with the helium fraction Y . Here $\phi(\nu, r)$ is the line profile at the radial distance r for the rest-frame frequency ν , which suffers the Doppler broadening due to the thermal velocity of the gas,

$$\phi(\nu, r) = \frac{1}{\Delta\nu\sqrt{\pi}} \exp\left(-\frac{(\nu - \nu_*)^2}{\Delta\nu^2}\right), \quad (30)$$

where the Doppler width $\Delta\nu$ is given by

$$\Delta\nu = \frac{\nu_*}{c} \sqrt{\frac{2k_B T_{\text{gas}}(r)}{m_H}}. \quad (31)$$

In equation (28), $\tau(\alpha_R)$ is obtained by $\tau(\alpha_R) = \tau(\alpha_R, R_{\text{max}})$. Hereafter, we set ν to $\nu = \nu_*$ [that is, the observed frequency is $\nu_{\text{obs}} = (1+z)\nu_*$]. We provide a comment about this setting in section 4.

To calculate equation (28) with equation (29), it is required to evaluate the spin temperature which is related to the ratio of the number densities of the two hyperfine structure levels. The spin temperature is given by (Field 1959),

$$T_s^{-1} = \frac{T_{\text{CMB}}^{-1}(z) + x_c T_{\text{gas}}^{-1} + x_\alpha T_\alpha^{-1}}{1 + x_c + x_\alpha}, \quad (32)$$

where T_α is the colour temperature of Ly α photons, and x_c and x_α represent the coupling coefficients for the gas collisions and the Ly α pumping, respectively. In this paper, we set $x_\alpha = 0$, because we assume that there exist no UV and X-ray external sources. The coupling coefficient for gas collisions is expressed in

$$x_c = \frac{T_*}{A_{10} T_{\text{CMB}}} C_{\text{Hi}}, \quad (33)$$

where C_{Hi} is the collisional coefficient between Hi atoms and we adopt the value in Kuhlen et al. (2006). Note that, since we assume that the gas inside UCMHs as fully neutral one, we neglect the contribution from the collisions of Hi with protons and electrons. Using equation (32) with the gas radial profile obtained in section 3.2, we obtain the radial profile of the spin temperature in the UCMHs for equations (28) and (29).

The effective brightness temperature averaged over the single UCMH cross-section, $\mathcal{S} = \pi r_{200}^2$, is given by

$$T_{b,zc} = \frac{\int T_b d\mathcal{S}}{\mathcal{S}} = 2 \int_0^1 T_b(\alpha_R) \alpha_R d\alpha_R. \quad (34)$$

We measure the 21-cm signals as the difference of the

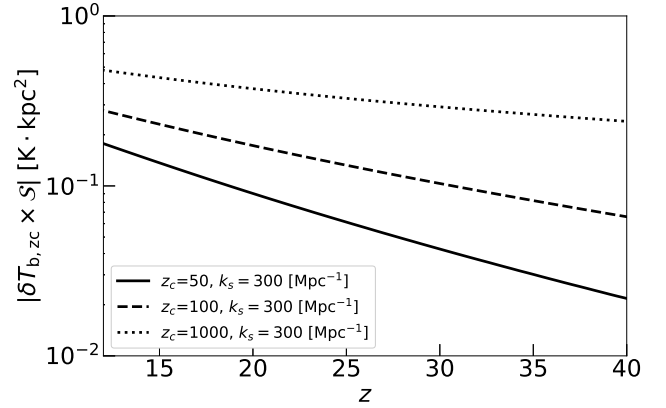


Figure 2. The 21-cm signal from a single UCMH, which is given by a product of the differential brightness temperature and a geometrical cross-section of UCMH, as a function of redshift. We show the 21-cm signal from a single UCMH at the formation redshift $z_c = 50, 100, 1000$ as the solid, dashed and dotted black lines, respectively.

brightness temperature from the CMB temperature, which is called the differential brightness temperature. The differential brightness temperature for the single UCMH at the redshift z can be calculated from

$$\delta T_{b,zc}(z) = \frac{T_{b,zc}}{1+z} - T_{\text{CMB}}(0). \quad (35)$$

Figure 2 provides the evolution of the 21-cm signal from the single UCMH. In this figure, the y -axis is the product of the differential brightness temperature and the UCMH cross-section, which corresponds to the total 21-cm flux from the single UCMH. Here we set $k_s = 300 \text{ Mpc}^{-1}$ which is smaller than k_J at $z = 10$. In this case, the signal is observed as emission on the CMB frequency spectrum. The 21-cm signal becomes strong as the baryon gas mass or temperature in the UCMH increases. Therefore, the signal monotonically becomes larger as the redshift decreases, because the UCMH virial mass grows logarithmically due to the accretion as shown in equation (8) even with fixing k_s .

In figure 2, we also show the dependence of the signal on the collapse redshift, z_c . UCMHs collapsed in higher redshifts have larger virial mass, according to equation (8). Hence, the UCMH with higher z_c provides the stronger signal, compared to the one with small z_c .

We plot the signal as a function of k_s in figure 3. The black lines represent the emission signals, while the red ones denote the absorption signal. Larger k_s provides UCMHs with small gas mass and low baryon gas temperature. Therefore, as k_s becomes larger, the spin temperature decreases and, then, the signal shifts from the emission to absorption because the averaged spin temperature cannot exceed the CMB temperature in such low UCMH mass. The figure also tells us that the signal radically decreases when k_s is larger than k_J . This is because the baryon with such k_s cannot collapse to the UCMH and the baryon gas mass fraction drops down as shown in figure 1.

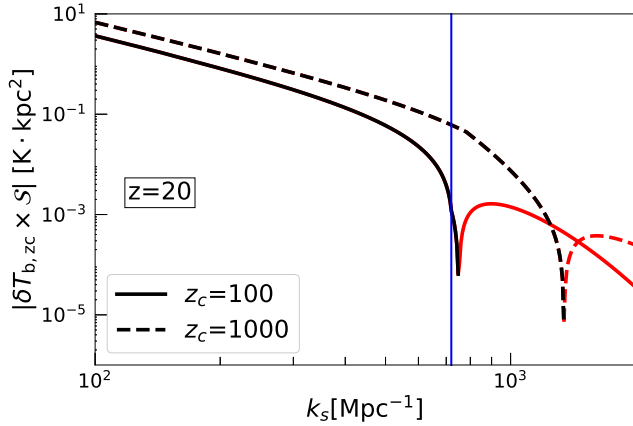


Figure 3. Dependence of the 21-cm signal from a single UCMH on the spike scale k_s . The solid and dashed lines correspond to the 21-cm signal from a single UCMH at $z_c = 100$ and 1000 , respectively. The vertical line shows the Jeans wave number at $z = 20$.

4 THE 21-CM FLUCTUATIONS DUE TO THE UCMH CLUSTERING

The angular scale of an individual UCMH on the sky is too small to be resolved even by upcoming 21-cm observations such as the SKA. Therefore, the key observable for the UCMHs is the differential brightness temperature fluctuations due to the number density fluctuation of UCMHs in the observational beam. In this section, we evaluate the rms fluctuations due to the UCMH as the 21-cm signal of UCMHs.

Now we consider the ensemble of UCMHs formed in the redshift from $z_{c,\max}$ to $z_{c,\min}$. Following [Iliev et al. \(2002\)](#), the mean 21-cm differential brightness temperature from this ensemble at the redshift z is given by

$$\overline{\delta T_b}(z) = \frac{c(1+z)^4}{\nu_* H(z)} \int_{z_{c,\min}}^{z_{c,\max}} \Delta\nu_{\text{eff}}(z) \delta T_{b,zc}(z) \mathcal{S} \frac{dn}{dz_c} dz_c. \quad (36)$$

Here we set $z_{c,\max} = 4000$ and $z_{c,\min} = 50$, and $\Delta\nu_{\text{eff}}$ is the effective linewidth, which is provided by

$$\Delta\nu_{\text{eff}}(z) = [\phi(\nu_*)(1+z)]^{-1} \approx \frac{\nu_*}{c(1+z)} \sqrt{\frac{2\pi k_B \overline{T}_{\text{gas}}(z)}{m_H}}, \quad (37)$$

where $\overline{T}_{\text{gas}}(z)$ is the volume averaged temperature within an individual UCMH. To calculate the mean 21-cm differential brightness temperature, it is required to evaluate the total flux integrated over the line profile. Instead of this integration, we take the rectangular approximation whose width is $\Delta\nu_{\text{eff}}$ and height is obtained by setting $\nu = \nu_*$ for the optical depth in equation (29) (for more detailed discussion, we refer readers to section 2 in [Iliev et al. 2002](#)).

On large scales, UCMHs are distributed homogeneously with the number density $n = \int dz_c dn/dz_c$. However, as the scale-invariant fluctuations on large scales evolve, the distribution of UCMHs can gravitationally trace this fluctuations on large scales. Therefore the number of UCMHs in an observational beam volume is fluctuated, depending on the matter density fluctuations in the beam. The rms fluctuations due to UCMHs can be evaluated by

$$\langle \delta T_b^2 \rangle^{1/2}(z) = \beta(z) \sigma_p(z) \overline{\delta T_b}(z), \quad (38)$$

where σ_p is the rms fluctuation of the matter density averaged in the observation beam volume. We adopt the cylinder-shape beam: the diameter and height of the cylinder-shape beam respectively correspond to the angular resolution, $\Delta\theta$, and the frequency resolution, $\Delta\nu$, of the observations. In this configuration, σ_p is given by

$$\sigma_p(z) = \int_0^\infty \frac{dk}{k} \mathcal{P}(k, z) W_{\text{cy}}(k, z), \quad (39)$$

where $\mathcal{P}(k, z)$ is the non-dimensional matter power spectrum at the redshift z . For the matter power spectrum, we use the amplitude $\sigma_8 = 0.81$ and the spectral index $n_s = 0.965$. The cylinder-shape beam window function is expressed in

$$W_{\text{cy}}(k, z) = \frac{16}{R^2 L^2} \int_0^1 dx \frac{\sin^2(kLx/2) J_1^2(kR(1-x^2)^{1/2})}{k^4 x^2 (1-x^2)}, \quad (40)$$

where R and L are the comoving radius and height of the cylinder, $R = \Delta\theta(1+z)D_A(z)/2$ and $L \approx (1+z)^2 c(\Delta\nu/\nu_*)/H(z)$.

In equation (39), $\beta(z)$ is the bias factor for the UCMH clustering to the matter density fields. We assume that β can be obtained by the flux weighted average of the linear bias over the different collapse redshifts,

$$\beta(z) = \frac{\int_{z_{c,\min}}^{z_{c,\max}} b \Delta\nu_{\text{eff}}(z) \delta T_{b,zc}(z) \mathcal{S} \frac{dn}{dz_c} dz_c}{\int_{z_{c,\min}}^{z_{c,\max}} \Delta\nu_{\text{eff}}(z) \delta T_{b,zc}(z) \mathcal{S} \frac{dn}{dz_c} dz_c}, \quad (41)$$

where b is the linear bias in the peak theory (see equation (24.b) with equations (17) and (25) in [Mo et al. 1997](#)). With the redshift decreasing, b is monotonically becomes small.

First we show the redshift evolution of the 21-cm fluctuations of UCMHs in the top panel of figure 4. When the redshift decreases, the fluctuations also become large as same as the single UCMH signal in figure 2. Note that we do not consider the impacts of cosmic reionization process. The abundant ionization photon background during the EoR can photoevaporate the neutral gas in UCMHs similarly to the case of minihaloes ([Iliev et al. 2005](#)). This photoevaporation suppresses the amplitude of the fluctuations near the EoR, $z \lesssim 10$.

In the top panel of figure 4, we also show the dependence of the fluctuations on the amplitude \mathcal{A}_ζ . The increment of \mathcal{A}_ζ enhances the fluctuations through two effects. The first one is to increase the number density of the UCMHs. However in our interested scales and redshifts, the number density is saturated when $\mathcal{A}_\zeta > 10^{-7}$. Hence, the enhancement through the number density is weak. The second one is that increasing \mathcal{A}_ζ results in the early-time formation of UCMHs. As shown in figure 2, the UCMHs forming in high redshifts provide large signals. This effect provides the dependence on \mathcal{A}_ζ in the top panel of figure 4.

The bottom panel in figure 4 shows the dependence on k_s for two different \mathcal{A}_ζ at $z = 20$. As k_s increases, the individual UCMH signal becomes small. Following its signals, the rms fluctuations also decline. When k_s is larger than the Jeans wave number, the signal rapidly drops down as expected from the section figure 3.

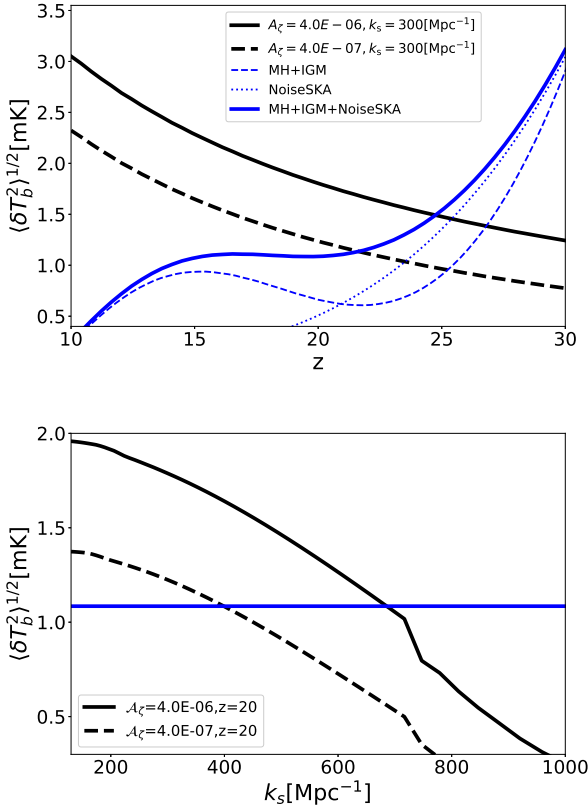


Figure 4. (Top panel) Redshift dependence of the 21-cm fluctuations from UCMHs. The black solid line and the dashed lines are the 21-cm fluctuations from UCMH for $A_\zeta = 4.0 \times 10^{-6}$ and 4.0×10^{-7} , respectively. In both lines, we set $k_s = 300 \text{ Mpc}^{-1}$. We also plot the fluctuation from the IGM + MHs in the blue dotted line, the SKA noise level in the blue dot-dashed line and the sum of them in the blue solid line. (Bottom panel) Dependence of the 21-cm fluctuations on the spike wave number k_s at $z = 20$. The solid line is for $A_\zeta = 4.0 \times 10^{-6}$ while the dashed line is for 4.0×10^{-7} . The blue solid line represents the fluctuation from the IGM + MHs with the SKA noise level.

4.1 Detectability with SKA

Several ongoing observations are attempting to detect the 21-cm fluctuation signal coming from $z \gtrsim 10$, e.g., LOFAR, GMRT, MWA, and Paper. Although there has been no report of the signal detection yet, some observations have provided upper limits on the 21-cm fluctuations, e.g., $\delta T_b^2(k) < (49.0 \text{ mK})^2$ at $k \approx 0.59 h \text{ Mpc}^{-1}$ at $z = 6.5$ by MWA (Li et al. 2019) and $\delta T_b^2(k) < (79.6 \text{ mK})^2$ at $k \approx 0.053 h \text{ Mpc}^{-1}$ at $z \sim 10$ by LOFAR (Patil et al. 2017).

However the maximum fluctuations by UCMHs in our model, $\delta T_b^2 \lesssim (5 \text{ mK})^2$ at $z = 20$, is fairly smaller than sensitivities of these instruments, we cannot provide the constraint on the UCMH abundance and the spike-shape power spectrum by the current performance of the 21-cm fluctuation observations.

The upcoming 21-cm observation, SKA, is expected to detect and measure the 21-cm fluctuations at $z \gtrsim 10$. We discuss the detectability of the 21-cm signals from UCMHs with the SKA. In this paper, to discuss the detectability for the 21-cm signal from UCMHs, we estimate the 21-cm

fluctuations by the IGM and minihaloes (MHs) and the observational noise of the SKA as well as the one by UCMHs.

In figure 4, we plot the expected fluctuations due to the IGM + MHs and the noise of SKA in the blue lines. For the detailed calculation of them, we refer the reader to the Appendix. We assume that the major contribution to the noise is the foreground emission of the sky. Since the foreground has the strong frequency dependence, the noise rapidly blows up as the redshift increases (the observation frequency decreases). In the frequency and angular resolutions of our interest, the noise becomes larger than the IGM + MH fluctuations above $z \sim 20$. Note that we ignore the effect of cosmic reionization, which might enhance the 21-cm fluctuations of the IGM below $z \sim 10$ based on the Planck constraint on Thomson scattering optical depth.

Our calculation has two free parameters related to the spike-shape spectrum, k_s and A_ζ , and the amplitude of the fluctuations depends on them. Taking the different parameter set, (k_s, A_ζ) , we survey the parameter region in which the 21-cm fluctuations of UCMHs can dominate the IGM + MH fluctuations and noise at $z = 20$. We show such parameter region as the red region in figure 5. When there exists the fluctuations due to the spike-shape spectrum in the red region, the SKA can detect the excess of the 21-cm fluctuations from the expected IGM + MH signals at $z = 20$. In other words, when the SKA does not find the excess of the 21-cm fluctuations, the delta-shape spectrum in the red region can be ruled out.

At $k_s \sim 700 \text{ Mpc}^{-1}$, one can see the sharp cutoff in figure 5. The cutoff scale corresponds to the Jeans scale at the observation redshift $z = 20$. When $k_s > k_J$, the baryon mass fraction radically drops down in UCMHs, in particular, which form late time. These UCMHs cannot host enough amount of the baryon gas to produce strong 21-cm signals for the detection. As a result, 21-cm observations cannot provide the constraint below the Jeans scale.

Although we show the constraint only with the observation redshift $z = 20$, it is worth mentioning about its dependence on the observation redshift. As shown in the top panel of figure 4, the fluctuation amplitude increases with the redshift decreases with fixing k_s . Therefore, when we take a redshift lower than $z = 20$, the constraint slightly becomes tighter. Moreover as the redshift decreases, the Jeans scale becomes small. Accordingly, the sharp cutoff of the allowed region on the high- k side shifts toward large k . When we perform the 21-cm observation at $z = 10$, we can extend the red region to $k_s \approx 1000 \text{ Mpc}^{-1}$ which corresponds to the Jeans scale at $z = 10$. However, in lower redshifts, the cosmological reionization process creates the additional 21-cm fluctuations as mentioned above. The additional fluctuations depend on the model of the reionization process. Therefore, it is difficult to evaluate the possible constraint on the primordial curvature amplitude with considering the reionization impact.

At the last of this section, we discuss the impact of the density profile on the 21-cm signals. In our calculation, we take the Moore profile and evaluate the gas density and temperature profiles based on the hydrostatic equilibrium. However, according to numerical simulations by Gosenca et al. (2017), if the UCMH formation occurs in non-isolated situations, the profile of the resultant UCMHs can be well fit by the NFW profile. To investigate the profile depen-

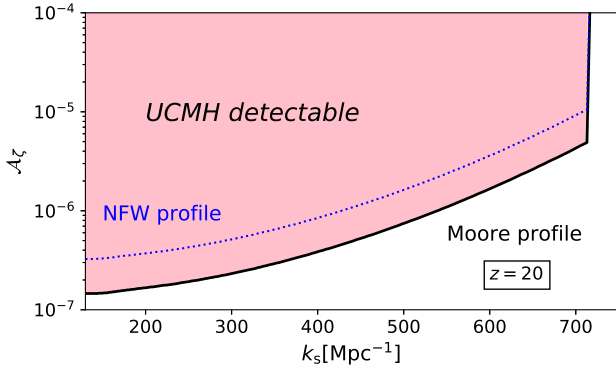


Figure 5. Detectability of the signal from UCMHs with observation by SKA. The spike-shape parameter in the red region can produce the 21-cm fluctuations due to UCMHs which can be observed by SKA. Here we set the observation redshift $z = 20$. The wave number on the left end of the red region corresponds to k_J . The dotted line represents the lower bound for the detection, when a UCMH dark matter distribution takes the NFW profile.

dence on the 21-cm signal, we simply adopt the NFW profile as the dark matter density distribution with using equations (4) and (5), and evaluate the signal taking the procedure in section 3 and 4. Since the NFW profile has a shallower slope in the inner region than the Moore profile, the signal from the NFW halo is weaker than that from the Moore halo. We plot the critical amplitude for the detection in the blue dotted line in figure 5. In short, when a UCMH has a shallower profile, the constraint on the spike-shape amplitude becomes loose.

5 CONCLUSION

UCMHs are originated in the density fluctuations with the spike-shape spectrum on small scales. Therefore, the observational limit on the UCMH abundance leads the upper bound on the small-scale power spectrum of the primordial fluctuations. In this paper, we have evaluated the 21-cm signals from the UCMHs and have demonstrated that the SKA can provide the upper limit on the abundance of the UCMHs as well as the small-scale primordial fluctuations.

Since the 21-cm signal depends on the distribution of baryon gas in UCMHs, we have constructed the theoretical model of the baryon gas density and temperature, taking the Moore profile as the dark matter density distribution in UCMHs. Then we are first to have calculated the 21-cm signal from an individual UCMH. As a result, we have found that the individual signal becomes large as the UCMH mass increases.

Our observable are the 21-cm fluctuations caused by the number density fluctuations of UCMHs. We have investigated a relation between the 21-cm fluctuations and the spike-shape spectrum of the primordial fluctuations. We have shown that the 21-cm fluctuations by UCMHs become large as the amplitude of the spike-shape increases or the peak shifts to small scales. We also have found that the 21-cm fluctuations due to UCMHs are in an order of mK in the redshift range from $z = 10$ and 30. However, if the wave number of the spike-shape spectrum becomes smaller than

the Jeans scale, the baryon gas mass in a UCMH drastically decreases, leading to the significant decrement of the signal.

Though the 21-cm fluctuations by UCMHs does not reach the sensitivity of the current observational instruments, the SKA may detect the signal if there is the spike-shape spectrum we have discussed on the primordial power spectrum.

On the other hand, assuming non-detection of the signal by the SKA, an upper limit on the curvature perturbations is provided to $\mathcal{A}_\zeta \lesssim 10^{-6}$ on $100 \text{ Mpc}^{-1} \lesssim k \lesssim 1000 \text{ Mpc}^{-1}$. Constraints on the UCMH abundance and the spike-shape spectrum have been provided through the gamma-ray observation assuming a self-annihilation of dark matter particles in UCMHs. Note that the constraint by the gamma-ray observation strongly relies on a model of dark matter, e.g., the annihilation mechanism and the mass of dark matter. In contrast, the 21-cm emission is independent of these detailed properties of dark matter. Therefore, the probe of 21-cm fluctuations by future observations is expected to be a more robust survey of the primordial fluctuation on small scales.

ACKNOWLEDGEMENTS

Numerical calculations were partially carried out on clusters installed in Nagoya University. This work was supported by JSPS KAKENHI Grant Numbers JP17H01110 (KH, HT, TT) and JP18K03699 (KH).

APPENDIX A: 21-CM SIGNALS FROM IGM AND MHS

In this appendix, we give descriptions for construction of 21-cm signals from IGM and MHS. Here, we assume $x_\alpha = 0$ in Eq. (32) because we assume that no UV and X-ray sources exist in the Universe above $z = 20$.

IGM fluctuations

The mean differential brightness temperature of the IGM is given by (Madau et al. 1997)

$$\overline{\delta T_b} = 9.1 (1+z)^{1/2} \left(1 - \frac{T_{\text{CMB}}}{T_s}\right) \left(\frac{\Omega_b h}{0.33}\right) \left(\frac{\Omega_m}{0.27}\right)^{-1/2} \text{ mK}, \quad (\text{A1})$$

where we assume that the IGM is fully neutral. For the IGM spin temperature, we take the IGM gas temperature evolution with only the Compton heating.

The 21-cm signals spatially fluctuate, depending on the baryon density fluctuations. We assume that the baryon distribution follows the matter density fluctuations. Accordingly, the observed rms 21-cm fluctuations due to the IGM can be evaluated in

$$\langle \delta T_{b,\text{IGM}}^2 \rangle^{1/2} = \sigma_p(z) \overline{\delta T_b}, \quad (\text{A2})$$

where $\sigma_p(z)$ is given in equation (39).

In our evaluation, we do not take into account the contribution of the ionization fluctuation in the IGM. This contribution to the 21-cm fluctuations increases as the cosmological reionization proceeds. Therefore, our evaluation on the IGM fluctuations is underestimated around $z \sim 10$.

Minihalo fluctuations

minihaloes (MHs) are virialized objects with the virial temperature $T_{\text{vir}} < 10^4$ K. In the standard hierarchical structure formation, they form abundantly in high redshifts and are filled with neutral hydrogen atoms. Therefore MHs are promised sources of 21-cm signals in high redshifts (Iliev et al. 2002; Furlanetto & Oh 2006).

In figure 4, we evaluate the 21-cm fluctuations due to MHs in the same manner as in the case of UCMHs, except for the dark matter profile. It is predicted that the dark matter distribution in MHs can be described in the NFW profile. For the concentration parameter, $p_{\text{con}} \equiv r_{\text{vir}}/r_s$ in the NFW profile, we set (Seljak 2000)

$$p_{\text{con}} = \frac{10}{1+z_c} \left[\frac{M}{M_*(z=0)} \right]^{-0.2}, \quad (\text{A3})$$

Here $M_*(z)$ satisfies $\sigma(M_*, z) = \delta_c$ where $\sigma(M, z)$ is the dispersion of the density fluctuations smoothed with the top-hat filter of the radius corresponding to mass M at the redshift z . In the calculation, we assume that the mass range of MHs spans from the Jeans mass M_J to the virial mass with $T_{\text{vir}} = 10^4$ K.

Noise level of SKA

The noise level of an interferometer such as SKA is given with the observation wave length λ by Furlanetto et al. (2006)

$$\delta T_N(\lambda) = \frac{\lambda^2}{A_{\text{eff}} \Delta \theta^2} \frac{T_{\text{sys}}}{\sqrt{\Delta \nu t_{\text{obs}}}}, \quad (\text{A4})$$

where A_{eff} , t_{obs} and T_{sys} are the effective collecting area, the observational time, and the system temperature, respectively.

We are interested in low frequency observation, $\nu < 150$ Hz. In such low frequency region, the sky temperature is the dominant component on T_{sys} . We take the sky temperature at high Galactic latitude where the foreground is low in the sky,

$$T_{\text{sys}} \sim 180 \left(\frac{180 \text{ MHz}}{\nu} \right)^{2.6} \text{ K}. \quad (\text{A5})$$

Therefore, the noise level is given in

$$\delta T_N(\nu) = 0.507 \text{ mK} \left(\frac{8 \times 10^5 \text{ m}^2}{A_{\text{eff}}} \right) \left(\frac{20'}{\Delta \theta} \right)^2 \left(\frac{3 \text{ MHz}}{\Delta \nu} \right)^{1/2} \times \left(\frac{1000 \text{ h}}{t_{\text{obs}}} \right)^{1/2} \left(\frac{1+z}{21} \right)^{4.6}. \quad (\text{A6})$$

For SKA, we set $A_{\text{eff}} = 8 \times 10^5 \text{ m}^2$, $\Delta \theta = 20$ arcmin, $\Delta \nu = 3$ MHz and $t_{\text{obs}} = 1000$ h.

REFERENCES

- Ali Z. S., et al., 2015, *ApJ*, **809**, 61
 Bardeen J. M., Steinhardt P. J., Turner M. S., 1983, *Phys. Rev. D*, **28**, 679
 Bardeen J. M., Bond J. R., Kaiser N., Szalay A. S., 1986, *ApJ*, **304**, 15
 Barkana R., Loeb A., 2001, *Phys. Rep.*, **349**, 125
 Beardsley A. P., et al., 2016, *ApJ*, **833**, 102
 Bird S., Peiris H. V., Viel M., Verde L., 2011, *MNRAS*, **413**, 1717
 Bondi H., Hoyle F., 1944, *MNRAS*, **104**, 273
 Bowman J. D., et al., 2013, *Publ. Astron. Soc. Australia*, **30**, e031
 Bringmann T., Scott P., Akrami Y., 2012, *Phys. Rev. D*, **85**, 125027
 Chluba J., Erickcek A. L., Ben-Dayan I., 2012, *ApJ*, **758**, 76
 Chongchitnan S., Silk J., 2012, *MNRAS*, **426**, L21
 Clark H. A., Lewis G. F., Scott P., 2016, *MNRAS*, **456**, 1394
 Clark H. A., Iwanus N., Elahi P. J., Lewis G. F., Scott P., 2017, *J. Cosmology Astropart. Phys.*, **2017**, 048
 Delos M. S., Erickcek A. L., Bailey A. P., Alvarez M. A., 2018a, *Phys. Rev. D*, **97**, 041303
 Delos M. S., Erickcek A. L., Bailey A. P., Alvarez M. A., 2018b, *Phys. Rev. D*, **98**, 063527
 Dent J. B., Easson D. A., Tashiro H., 2012, *Phys. Rev. D*, **86**, 023514
 Emami R., Smoot G. F., 2018, *J. Cosmology Astropart. Phys.*, **2018**, 007
 Field G. B., 1959, *ApJ*, **129**, 536
 Furlanetto S. R., Oh S. P., 2006, *ApJ*, **652**, 849
 Furlanetto S. R., Oh S. P., Briggs F. H., 2006, *Phys. Rep.*, **433**, 181
 Gosenca M., Adamek J., Byrnes C. T., Hotchkiss S., 2017, *Phys. Rev. D*, **96**, 123519
 Guth A. H., Pi S.-Y., 1982, *Physical Review Letters*, **49**, 1110
 Iliev I. T., Shapiro P. R., Ferrara A., Martel H., 2002, *ApJ*, **572**, L123
 Iliev I. T., Shapiro P. R., Raga A. C., 2005, *MNRAS*, **361**, 405
 Josan A. S., Green A. M., 2010, *MNRAS*, **405**, 083527
 Josan A. S., Green A. M., Malik K. A., 2009, *Phys. Rev. D*, **79**, 103520
 Jungman G., Kamionkowski M., Griest K., 1996, *Phys. Rep.*, **267**, 195
 Kolb E. W., Chung D. J. H., Riotto A., 1999, in Klapdor-Kleingrothaus H. V., Baudis L., eds, *Dark matter in Astrophysics and Particle Physics*. p. 592 ([arXiv:hep-ph/9810361](https://arxiv.org/abs/hep-ph/9810361))
 Komatsu E., Seljak U., 2001, *MNRAS*, **327**, 1353
 Komatsu E., Seljak U., 2002, *MNRAS*, **336**, 1256
 Koopmans L., et al., 2015, in *Advancing Astrophysics with the Square Kilometre Array (AASKA14)*. p. 1 ([arXiv:1505.07568](https://arxiv.org/abs/1505.07568))
 Kuhlen M., Madau P., Montgomery R., 2006, *ApJ*, **637**, L1
 Li F., Erickcek A. L., Law N. M., 2012, *MNRAS*, **426**, 043519
 Li W., et al., 2019, *ApJ*, **887**, 141
 Loeb A., Zaldarriaga M., 2004, *Phys. Rev. Lett.*, **92**, 211301
 Mack K. J., Wesley D. H., 2008, *arXiv e-prints*, p. [arXiv:0805.1531](https://arxiv.org/abs/0805.1531)
 Madau P., Meiksin A., Rees M. J., 1997, *ApJ*, **475**, 429
 McDonald P., et al., 2006, *ApJS*, **163**, 80
 Mo H. J., Jing Y. P., White S. D. M., 1997, *MNRAS*, **284**, 189
 Moore B., Quinn T., Governato F., Stadel J., Lake G., 1999, *MNRAS*, **310**, 1147
 Nakama T., Suyama T., Kohri K., Hiroshima N., 2018, *Phys. Rev. D*, **97**, 023539
 Navarro J. F., Frenk C. S., White S. D. M., 1995, *Monthly Notices of the Royal Astronomical Society*, **275**, 720
 Paciga G., et al., 2011, *MNRAS*, **413**, 1174
 Paciga G., et al., 2013, *MNRAS*, **433**, 639
 Parsons A. R., et al., 2010, *AJ*, **139**, 1468

- Patil A. H., et al., 2017, *ApJ*, **838**, 65
- Planck Collaboration et al., 2018, arXiv e-prints, p. [arXiv:1807.06211](#)
- Ricotti M., Gould A., 2009, *ApJ*, **707**, 979
- Scott P., Sivertsson S., 2010, *Phys. Rev. Lett.*, **105**, 119902
- Sekiguchi T., Takahashi T., Tashiro H., Yokoyama S., 2018, *J. Cosmology Astropart. Phys.*, **2018**, 053
- Sekiguchi T., Takahashi T., Tashiro H., Yokoyama S., 2019, *J. Cosmology Astropart. Phys.*, **2019**, 033
- Seljak U., 2000, *MNRAS*, **318**, 203
- Steigman G., Turner M. S., 1985, *Nuclear Physics B*, **253**, 375
- Suto Y., Sasaki S., Makino N., 1998, *ApJ*, **509**, 544
- Tashiro H., Sugiyama N., 2013, *MNRAS*, **435**, 3001
- Tingay S. J., et al., 2013, *Publ. Astron. Soc. Australia*, **30**, e007
- Tselikhovich D., Hirata C., 2010, *Phys. Rev. D*, **82**, 083520
- Yang Y., 2016, *European Physical Journal Plus*, **131**, 432
- Yang Y., Feng L., Huang X., Chen X., Lu T., Zong H., 2011, *J. Cosmology Astropart. Phys.*, **2011**, 020
- Yang Y., Yang G., Zong H., 2013, *Phys. Rev. D*, **87**, 103525
- Zhang D., 2011, *MNRAS*, **418**, 1850
- van Haarlem M. P., et al., 2013, *A&A*, **556**, A2